

Optimal chirality enhances long-range fluctuation-induced interactions in active fluids

Hashem Fatemi,¹ Hamidreza Khalilian,¹ Jalal Sarabadani,¹ and M. Reza Shaebani²

¹*School of Nano Science, Institute for Research in Fundamental Sciences (IPM), 19395-5531 Tehran, Iran*

²*Department of Theoretical Physics and Center for Biophysics,
Saarland University, 66123 Saarbrücken, Germany*

Understanding how chiral active particles— which self-propel and self-rotate— interact with each other is crucial to uncover how chiral active matter self-organizes into dynamic structures and patterns. Long-range fluctuation-induced (FI) forces in nonequilibrium steady states of active matter systems can be considerably strong and govern structure formation in interplay with other interactions. However, the impact of chirality on FI forces is not understood to date. We study effective forces between intruders immersed in chiral active fluids with tunable chirality and find that the influence of chirality on the FI force nontrivially depends on the elongation of active particles. By increasing the ratio between self-rotation and self-propulsion, the FI force monotonically decreases for fully circular active objects, as the active bath structure gradually changes from rotating flocks and vortices to localized spinners. Contrarily, a nonmonotonic behavior is observed upon increasing the chirality of rodlike active objects: There exists an optimal chiral angle which maximizes the magnitude and range of the FI interaction. We obtain the phase diagram of transition between attractive and repulsive forces in the space of chirality, propulsion, and separation between intruders. By measuring the collision statistics between active particles and intruders at different chirality and separation, we establish a direct link between the FI force and the average collision number and demonstrate how the balance of collisions around the intruders varies with chirality and separation. Our results provide new insights into an interplay between activity, chirality, and self assembly.

Formation of patterns and structures is among the most remarkable features of active matter systems [1–4]. Over the past two decades, there has been significant progress in our understanding of such phenomena— including, e.g., segregation, self-assembly, and clustering in active-passive mixtures [5–7], motility-induced phase separation [1], and emergence of effective interactions in confined active fluids [8, 9] and actomyosin gels [10, 11]. Most studies have concentrated on linear (i.e. non-chiral) self-propelled particle systems, where rotational symmetry holds in general as particles randomly rotate due to collisions or noise. In this class of active matter, the physics is governed by combined effects of propulsion, inherent or environmental noise, and nonlinearity and multiscale nature of interparticle interactions.

Nevertheless, lack of mirror symmetry is ubiquitous in living and nonliving active systems. Examples of chiral active motion range from clockwise [12–15] or counterclockwise [16] circular motion of flagellated bacteria close to surfaces or interfaces and helical swimming of marine zooplankton [17] and sperm cells [18, 19] to circular motion of synthetic self-propelled objects with asymmetric shape [20, 21] or mass distribution [22] with respect to their propulsion axis. Coupling of translational and rotational modes of active motion is known to optimize navigation [23–25] and induce gearlike rolling in dense confined geometries [26, 27], suggesting that the coupling may also affect fluctuation-induced forces generic to nonequilibrium systems [28, 29]. To get insight into how chiral active matter organizes into dynamic patterns and structures [30, 31], a detailed understanding of the interplay between active rotation and other key aspects of the problem is crucial, which is currently lacking.

Fluctuation-induced (FI) forces act on different length scales in nonequilibrium systems of driven passive [32–34] or active [35–43] particles. In contrast to relatively weak FI forces in passive environments, these forces can grow arbitrarily large with increasing self-propulsion in active systems [35]. The FI force also depends on bath density, noise strength, and size, shape, and orientation of intruders immersed in the active fluid and the separation between them [32, 34–37, 41, 42]. Moreover, switching between attractive and repulsive forces have been observed upon varying the bath density or separation and size of the intruders [32, 35–38]. Whether and how the interplay of FI forces and other interactions can prevent or promote formation of structures in chiral active matter systems has remained unexplored to date. The subject is of fundamental and practical importance as, for example, in biofilm formation and design of micro-devices [44] and active chiral crystals [45–47]. A major step towards answering the above questions is to uncover how FI forces are influenced by chirality, a still poorly understood issue [38].

Here we study effective interactions between immobile intruders immersed in chiral active fluids (Fig. 1A). Using extensive Langevin dynamics simulations we show that the intruders experience an effective long-range force beyond the depletion interaction range. The sign of the FI force in a non-chiral bath switches depending on the forward propulsion of the particles and the separation between the intruders. The maximum size of the force scales nearly linearly with forward propulsion, thus, the FI force can grow arbitrarily large and be competitive with other interactions in the system to form structures. To study the effect of chirality, we hypothesized that the

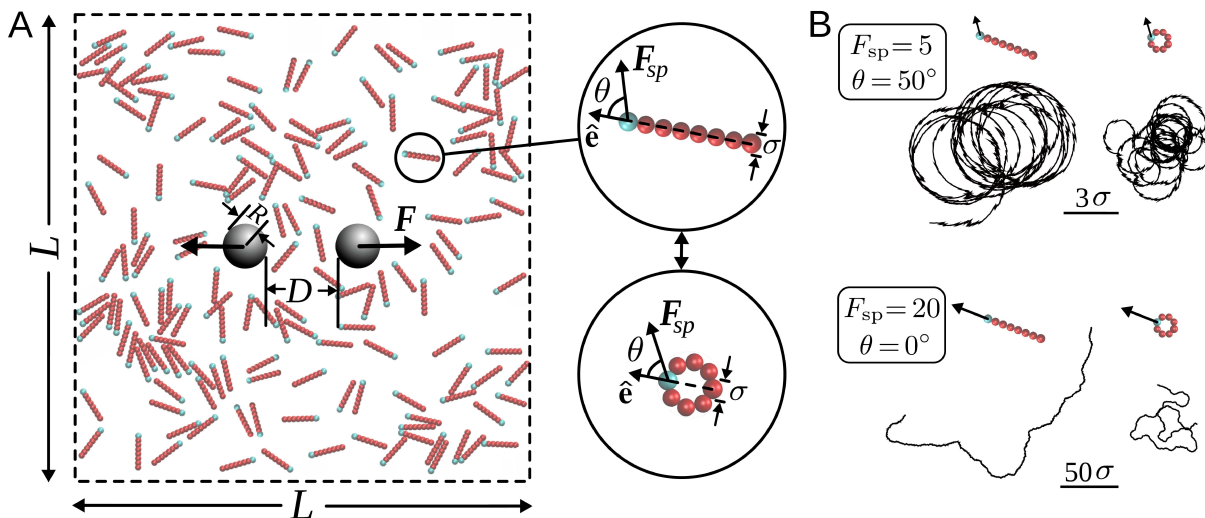


FIG. 1. **Schematic of the simulation box.** (A) Typical snapshot of the system with area fraction $\phi = 0.1$. Immobile (gray) intruders are immersed in an active bath consisting of either rodlike or circular rigid composites of beads as displayed in the insets. The self-propulsion (active) force \mathbf{F}_{sp} is exerted on the head (blue) bead with the self-propulsion angle (chirality) θ with respect to the intrinsic orientation $\hat{\mathbf{e}}$ of the active object. (B) Sample trajectories of active objects during the same time interval for different choices of chirality θ and magnitude of active force F_{sp} (in $k_B T / \sigma$ units).

elongation of active particles should play a crucial role as, for example, pure rotation of particles in a dense environment leads to localized spinning of circular particles while induces correlated rotations in case of interacting rods. To disentangle the effects from chirality and shape elongation on the FI force we consider two extreme limits of elongation for active objects, a fully circular or a rodlike elongated shape. Our results show that, under the same conditions, rodlike particles develop stronger FI forces. The interaction range, however, depends on the chiral angle; we uncover a nonmonotonic dependence on chirality in active baths of elongated particles, which allows for optimizing FI interactions in chiral active systems with tunable chirality. How the combination of chirality, propulsion, separation, and density affects the sign of the effective force is also addressed.

We construct rigid composites of touching beads of diameter σ arranged either on a straight line or on a circular ring; see Fig. 1A. These composite objects constitute the elements of the bath. We consider a two dimensional system motivated by chiral in-plane motion of biological and synthetic agents above surfaces [12–16, 20, 21]. Periodic boundary conditions are imposed in both directions and two immobile circular intruders of radius $R = 5\sigma$ are immersed with separation D . By exerting a self-propulsion force \mathbf{F}_{sp} on each composite particle, the bath changes from a passive to an active fluid with a tunable forward propulsion. \mathbf{F}_{sp} is applied on the head bead of the rod or a chosen bead of the circular object (blue beads in Fig. 1A). The chirality is tuned by changing the angle θ between \mathbf{F}_{sp} and the intrinsic orientation $\hat{\mathbf{e}}$ of the active object (i.e. the line symmetrically dividing the

composite through the blue bead). The choice of $\theta = 0$ ($\theta \neq 0$) corresponds to a non-chiral (chiral) active fluid.

The intruders and the constituent elements of the active/passive bath are assumed to be rigid; thus, an exclusion interaction between particles is introduced through the Weeks-Chandler-Andersen potential [48]

$$U_{wca}(d) = \begin{cases} U_{LJ}(d-\Delta) - U_{LJ}(d_c) & \text{if } d - \Delta < d_c, \\ 0 & \text{if } d - \Delta \geq d_c, \end{cases} \quad (1)$$

with d being the center-to-center distance between the interacting objects, U_{LJ} the Lennard-Johnes potential, and $d_c = 2^{1/6}\sigma$ the cut-off distance. Δ equals 0 or $R - \sigma/2$ for bead-bead (of different particles) or bead-intruder interaction, respectively. The position \mathbf{r}_i of the i th bead of each composite object evolves according to the Langevin equation

$$M \ddot{\mathbf{r}}_i = -\eta \dot{\mathbf{r}}_i - \nabla U_i + \boldsymbol{\xi}_i + \mathbf{F}_{sp,i} \delta_{hi}, \quad (2)$$

where M , η and U_i are the mass of each bead, solvent friction, and sum of all interactions acting on the i th bead, respectively. The random force $\boldsymbol{\xi}_i$ is a Gaussian white noise with zero mean and correlation $\langle \xi_{i,a}(t) \xi_{j,b}(t') \rangle = 4\eta k_B T \delta_{ab} \delta(t-t')$, in which a and b denote Cartesian components of the vectors, k_B the Boltzmann constant, and T the temperature. The constraint that the active force only acts on the head (h) bead is enforced by the Kronecker delta in the last term. A few examples of the resulting particle trajectories at area fraction $\phi = 0.1$ are shown in Fig. 1B. It is known that increasing self-propulsion enhances forward motion and the asymptotic diffusion coefficient of non-interacting active agents [49, 50], while inducing asymmetry in propulsion reduces the diffusion coefficient and leads to spiral

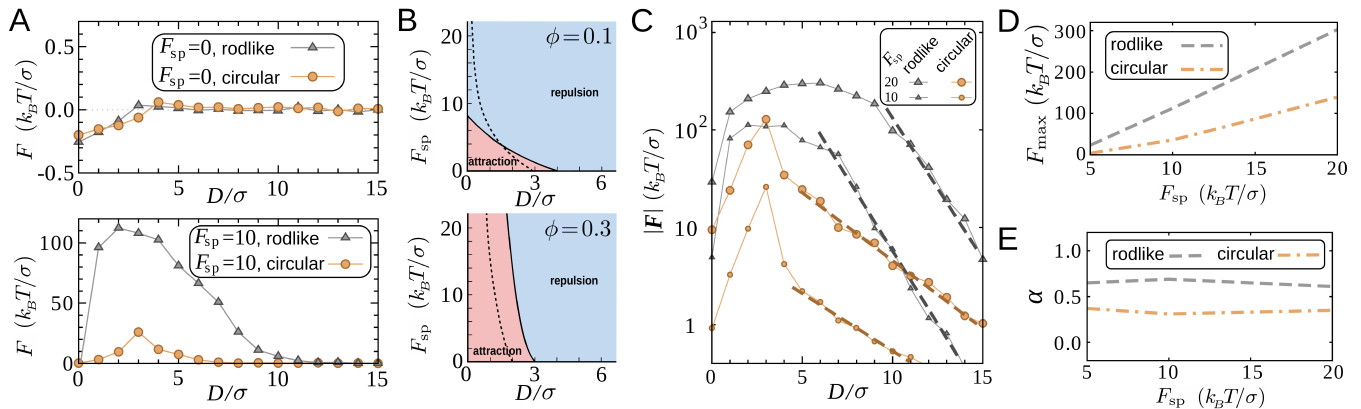


FIG. 2. **FI forces in non-chiral active fluids.** (A) FI force F between the intruders in a bath of passive ($F_{sp} = 0$; top panel) or active ($F_{sp} = 10 k_B T / \sigma$; bottom panel) non-chiral ($\theta = 0$) objects in terms of the gap size D between the intruders (scaled by the bead diameter σ). Error bars are smaller than symbols. The area fraction is $\phi = 0.1$. (B) Phase diagram of force sign switching in the (D, F_{sp}) plane for $\phi = 0.1$ (top) and 0.3 (bottom). The solid (dashed) line marks the interface position for circular (rodlike) active objects. (C) F versus D for different values of F_{sp} at $\phi = 0.1$. The dashed lines represent the best exponential fit to the asymptotic tail. (D, E) Maximum force F_{max} (panel D) and decay exponent α (panel E) versus F_{sp} at $\phi = 0.1$ for rodlike and circular active particles.

trajectories [51]. Similar trends are observed here upon varying the active force and chirality at low densities of the active bath. In the nonequilibrium steady state we measure the net force exerted by the active fluid on each intruder along the line which connects their centers. The force acting on the right intruder is denoted by \mathbf{F} in the following. Because of large fluctuations, the force is measured for 10^4 successive time intervals in the steady state and ensemble averaged over 10^2 uncorrelated trajectories; see *Materials and Methods* for details.

FI forces in non-chiral active fluids

We first consider non-chiral active fluids (i.e. $\theta = 0$). The resulting FI force in a passive fluid ($F_{sp} = 0$) is relatively weak ($F < 1 k_B T / \sigma$) and switches from attraction to repulsion with increasing the separation D between the intruders; see Fig. 2A (upper panel). The sign switching of the force upon increasing the gap between the intruders is in agreement with previous reports of emerging FI interactions in passive baths of spherical beads interacting with nearly elastic collisions (large restitution coefficient limit) [32, 33].

In comparison, the FI force can be arbitrarily stronger in active fluids ($F_{sp} \neq 0$). An example is shown in the lower panel of Fig. 2A for $F_{sp} = 10 k_B T / \sigma$, where F exceeds $100 k_B T / \sigma$ for rodlike active particles. Our results also reveal a novel feature in active fluids: The FI force behaves nonmonotonically as a function of the separation between the intruders. It first develops a peak F_{max} — at a value of D which can be beyond the short depletion range — and then decays. F_{max} is stronger for rodlike particles than for circular ones. However, the interac-

tions in circular-particle non-chiral fluids decay slower, i.e., remain efficient over longer distances (see below).

For sufficiently small active forces, the sign of the FI force is reversed (from attraction to repulsion) upon increasing D , similar to the behavior in passive fluids. With increasing F_{sp} , the crossover separation D_c (at which the sign changes) decreases and eventually vanishes; thus, F becomes purely repulsive for strong self-propulsions. One also expects that the active bath density ϕ influences the transition, as it has been shown to affect the forces acting on passive objects in active baths [8] (Moreover, sign reversal of the effective force acting on intruders was reported to be density-dependent in passive baths [32, 33]). Here we observe that with increasing bath density ϕ , the transition to pure repulsion is postponed to larger F_{sp} values. Figure 2B summarizes the sign switching behavior of the FI force in the (D, F_{sp}) plane at two different bath densities of either circular or rodlike particles.

Figure 2C shows a log-lin plot of F versus D for circular and rodlike particles at different F_{sp} values. Increasing F_{sp} enhances the FI force (and slightly shifts the peak position to larger separations in case of rods). The peak value F_{max} grows nearly linearly with F_{sp} ($F_{max} \propto F_{sp}$) as shown in Fig. 2D. The unbounded growth of the FI force with increasing F_{sp} points to possible relevance of it for self-organization and assembly in active matter systems. We checked that under the same conditions, $F_{max}^{circular} < F_{max}^{rodlike}$ always holds in non-chiral active baths; i.e., elongation of active particles increases F_{max} in general. The difference between the FI forces induced by rodlike or circular particles even grows with F_{sp} (different slopes in Fig. 2D). The tail behavior of F versus D can be roughly captured by an exponential decay $F_{tail} \sim e^{-\alpha D / \sigma}$. The decay slope α does not show

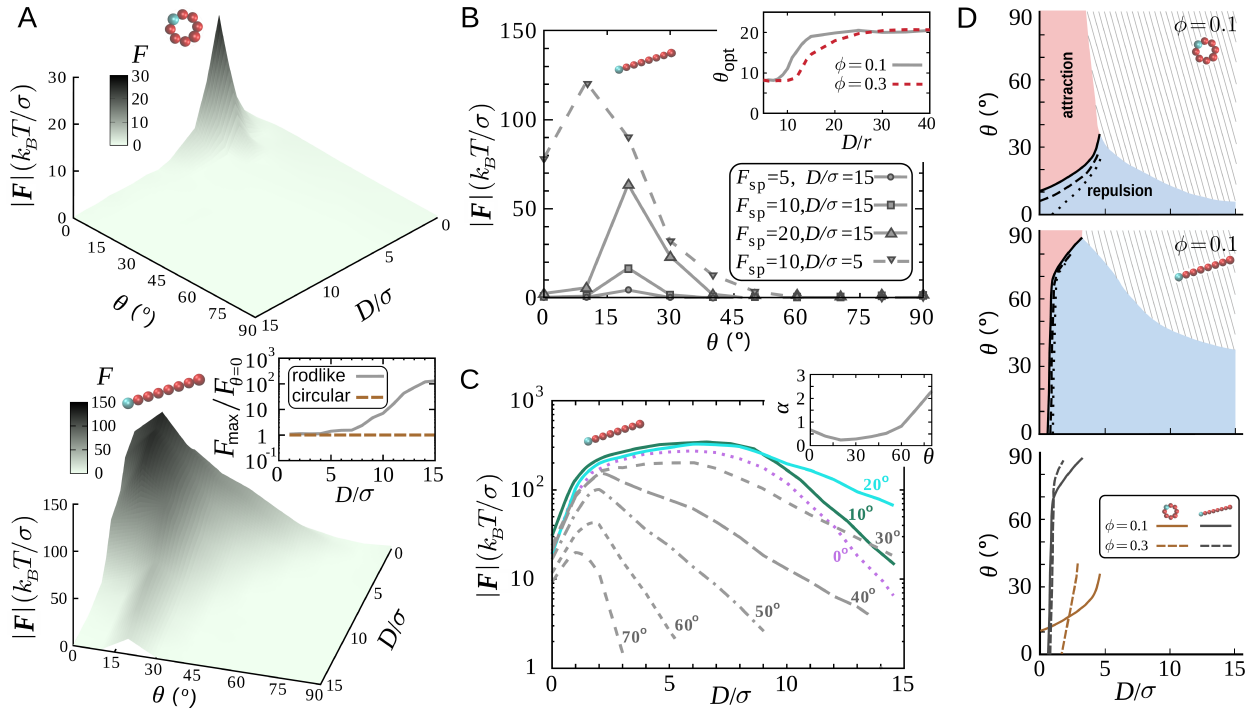


FIG. 3. **FI forces in chiral ($\theta \neq 0$) active fluids.** (A) FI force F in terms of scaled gap size D/σ and chiral angle θ at $F_{\text{sp}} = 10 k_B T/\sigma$ and $\phi = 0.1$ for circular (top) and rodlike (bottom) active objects. The inset shows the ratio between the maximum FI force F_{max} and the non-chiral FI force $F_{\theta=0}$ at different values of D/σ for circular and rodlike objects. (B) F versus θ in active baths of rodlike objects with $\phi = 0.1$ for different values of F_{sp} and D/σ . Inset: Optimal chiral angle θ_{opt} versus D/σ for different bath densities. (C) F versus D for rodlike active particles at different values of chirality θ . Other parameters: $F_{\text{sp}} = 10 k_B T/\sigma$, $\phi = 0.1$. Inset: Decay exponent α of the exponential fit to the F - D tail behavior in terms of θ . (D) Phase diagram of force sign switching in the (D, θ) plane for $F_{\text{sp}} = 20$. The upper and middle panels represent the diagram for active chiral baths of circular or rodlike particles, respectively. The solid line marks the interface for $F_{\text{sp}} = 20 k_B T/\sigma$. The interface position is also shown for $F_{\text{sp}} = 10$ (dashed line) and $5 k_B T/\sigma$ (dotted line). The hatched zones correspond to weak FI forces where random sign reversals occur within the accuracy of our measurements. The lower panel represents a comparison between the interface positions at bath densities $\phi = 0.1$ and 0.3 for $F_{\text{sp}} = 20 k_B T/\sigma$.

a systematic dependence on F_{sp} for both types of bath particle shapes; see Fig. 2E. Moreover, α is smaller for circular particles corresponding to a longer interaction range. We checked that the conclusions are independent of the choice of bath density.

FI forces in chiral active fluids

In order to see whether the FI force is influenced by chirality, we vary the chiral angle θ and measure F for different gap sizes D between the intruders. Interestingly, the results reveal that the impact of θ on F depends on the elongation of active particles. For circular particles, increasing θ monotonically weakens F (Fig. 3A). It means that for any given separation D , the intruders in an active fluid with circular constituent elements experience the maximum FI force in the non-chiral case ($\theta = 0$). Contrarily, in case of rodlike active particles F behaves nonmonotonically upon increasing θ ; it develops a peak at a nonzero chiral angle θ_{opt} and decays at larger chi-

ral angles. The inset of Fig. 3A shows that the relative strengthening of F compared to the non-chiral case is enhanced with increasing D . At large separations, where the FI force in the non-chiral case is weak, adopting the optimal chiral angle can strengthen the force by several orders of magnitude.

In Fig. 3B, we plot F versus θ for different values of F_{sp} and D at bath density $\phi = 0.1$. It can be seen that the optimal chiral angle θ_{opt} is independent of the choice of self-propulsion force. In addition, θ_{opt} slightly grows with D at small separations but eventually saturates to $\theta_{\text{opt}} \simeq 20^\circ$ at larger D values (inset of Fig. 3B). Similar conclusions are drawn for other values of bath density, though, the transition to asymptotic θ_{opt} shifts to larger D values with increasing ϕ .

The optimal chirality also remarkably enhances the range of FI interactions. Figure 3C shows F in terms of D for different values of θ . Similar to the behavior observed in non-chiral active fluids (shown in Fig. 2C), the tail of the FI force versus D can be approximated by an exponential decay $F_{\text{tail}} \sim e^{-\alpha(\theta) D/\sigma}$ for each choice of

the chiral angle. The decay slope α depends on the chirality: As shown in the inset of Fig. 3C, by adopting a chiral angle around the optimal angle θ_{opt} , α reaches a minimum value corresponding to the longest range for the FI interaction.

In chiral active fluids, the sign of the FI force is determined in general by the interplay of chirality, self-propulsion, bath density, and separation between the intruders. In Fig. 3D, we present a cut through the phase diagram of FI force sign reversal, where the separation and chirality are changed. For both circular and rodlike active particles, increasing θ shifts the transition from attraction to repulsion to larger separations. F_{sp} acts in the opposite direction, i.e., pushes the repulsive force zone to smaller D values (more pronounced for circular active particles); see top and middle panels of Fig. 3D. This trend is similar to the one observed in non-chiral baths. The impact of bath density on the force sign depends on the chirality of the active particles: At small values of θ , increasing ϕ enhances the attractive force domain. The effect is more pronounced for circular active particles. In contrast, increasing ϕ at large chiral angles reduces the attraction domain to smaller separations (lower panel). We note that the hatched zones in the phase diagrams of Fig. 3D mark the regions where the FI force is too weak ($F \lesssim 0.1 k_B T/\sigma$) and random sign switchings occur within the accuracy of our time-consuming measurements. Increasing F_{sp} or ϕ strengthens the FI force and pushes the hatched zone to the right, i.e., larger separations.

DISCUSSION

To obtain a qualitative understanding of the physical processes underlying the generation of FI forces in chiral active systems, studying the distribution of thermodynamic fields around the intruders is crucial. In randomly driven passive baths, it was shown that the presence of large intruder objects modifies the pressure field fluctuations in the inner regions between the intruders due to the boundary conditions imposed by them; this leads to effective long-range interactions [32, 33]. It has also been shown recently that a probe in the vicinity of lateral walls in an active fluid experiences an effective force which is directly related to the uneven density of active particles around the probe [8]. Here we extract the statistics of collisions between the intruders and active particles, which is a direct indicator of imbalance in thermodynamic fields around the intruders.

Our novel observation of a nonmonotonic dependence of the FI force on the separation between the intruders appears to be specific to baths of active particles. A plausible assumption is that the behavior originates from a similar (i.e. nonmonotonic) D -dependence of the collision imbalance around the intruders. To elucidate the roles of separation between the intruders and activity on col-

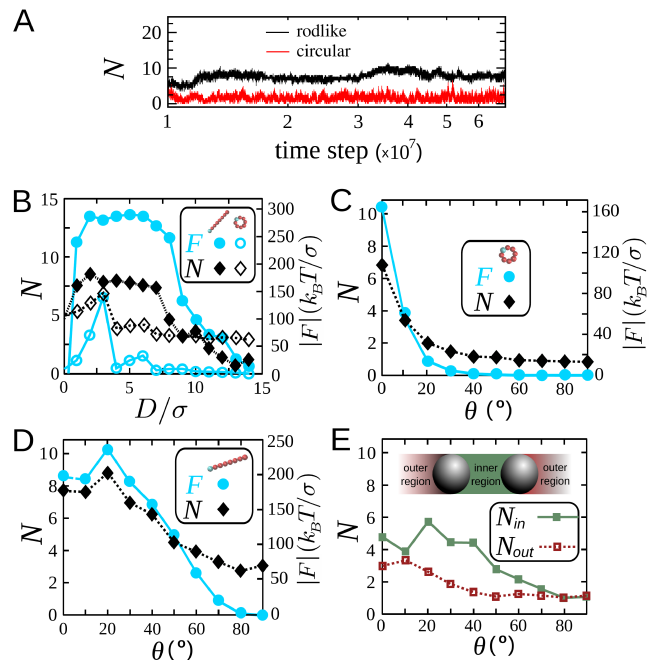


FIG. 4. **Statistics of collisions between active particles and intruders.** (A) Time evolution of the number of collisions between the right intruder and active particles in the steady state (time steps $> 10^7$), for $\phi = 0.3$, $D/\sigma = 8$, $F_{\text{sp}} = 20 k_B T/\sigma$, and $\theta = 20^\circ$. (B) Mean number of collisions N with the right intruder (per 10^3 time steps) as well as the FI force F in terms of D for both rodlike and circular particles at $F_{\text{sp}} = 20 k_B T/\sigma$, $\phi = 0.1$, and $\theta = 0$. (C,D) N and F versus θ for $F_{\text{sp}} = 20 k_B T/\sigma$. Other parameters: $\phi = 0.3$, $D/\sigma = 3$, circular objects (C); $\phi = 0.1$, $D/\sigma = 2$, rods (D). (E) Number of collisions between rodlike active particles and the right intruder as in panel (D) but separately presented for collisions in the inner and outer regions between the intruders shown in the inset.

lision statistics, we draw attention to the target-finding efficiency of active particles in confinement: It is known that the mean time to hit a random target by an active searcher (equivalently the cover time to scan the entire confined space) adopts a minimum at an optimal intermediate confinement size (compared to the given persistence length of the searcher) [23]. Thus, upon increasing D the random hitting time in the inner confined region between the intruders reaches a minimum (corresponding to a maximum collision frequency). In the outer region, variation of D has less impact on the relative change of the confinement size and, thus, on the particle-intruder collision statistics. The optimal separation D_{opt} is expected to grow with F_{sp} (as the persistence length of the active particles increases), which is consistent with the rodlike particle data in Fig. 2C, though the shift in the peak position is small for circular particles.

To validate our key assumption of a direct connection between the FI force and particle-intruder collisions, we measure the number of collisions with intruders in

the steady state (Fig. 4A). Typical examples of the D -dependence of F and the mean number of collisions N for both particle elongations are shown in Fig. 4B; it demonstrates that F and N are highly correlated with each other.

The nonmonotonic dependence of F on θ in chiral active fluids consisting of rodlike particles also originates from the similar behavior of N with θ . When comparing the particle-intruder collision statistics in circular and rodlike active fluids (examples are shown in Figs. 4C,D), we observe a gradual decay of N with θ for circular particles while N reaches a peak value for rodlike particles similar to the behavior of F . The strong correlation between the θ -dependence of F and N establishes again a direct link between them. By separating the collisions of rods with intruders in the inner and outer regions in Fig. 4E, we verify that the nonmonotonic behavior of N versus θ is induced by the collisions in the inner region.

The elongation dependence of the number of collisions points to possible differences between the dynamics of individual circular and rodlike particles. When the driving force and the intrinsic orientation of the active particle are not aligned, on one hand, forward propulsion weakens which reduces the directional correlation length in the system [52]. This, however, affects circular and rodlike objects in a similar way. On the other hand, a torque is exerted leading to self-rotation and spiral trajectories, as shown in Fig. 1B. Such a torque is caused, e.g., by viscous forces acting on the cell body and flagella of swimming bacteria near surfaces, which modify the pressure and velocity fields around the bacteria. The radius of curvature of the resulting circular motion increases with the bacterium cell-body length [13, 16]. For artificial microswimmers with asymmetric shapes, radius of curvature was found to be independent of the propulsion strength but it depends on the asymmetry of the particle shape [20]. The larger radius of spiral trajectories for rods compared to circles at the same chiral angle induces stronger correlated dynamics and larger FI forces in active chiral baths of rodlike particles. Moreover, with increasing the chirality towards $\theta=90^\circ$ (absence of forward propulsion), motion of rodlike particles remains highly entangled due to gearlike rollings while the patterns of motion in active circular-particle baths gradually change from vortices and rotating flocks to localized spinning [53] and the active objects eventually turn to isolated active spinners which rotate without a net displacement [45].

We finally note that the unidirectional rotation of the active particles in the chiral bath exerts a net torque on each intruder [54] and induces a gearlike rotation (even in case of a single intruder surrounded by isotropic collisions): We find an imbalance between the horizontal force (i.e. along the x -axis in Fig. 5) exerted on the upper and lower halves of each intruder ($\Delta F_x = |F_x^{\text{up}} - F_x^{\text{low}}| > 0$). Similarly, collisions exert unequal net forces in the per-

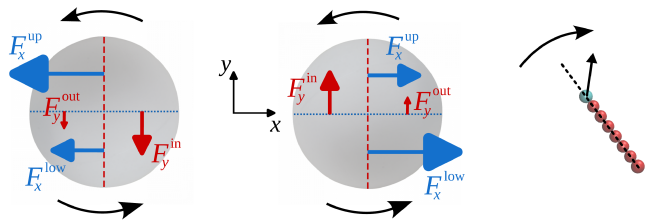


FIG. 5. **Schematic of the FI force components.** The inner and outer (upper and lower) halves of each intruder are separated by the red dashed (blue dotted) lines. Examples of net force imbalances between different halves are: $\Delta F_x = |F_x^{\text{up}} - F_x^{\text{low}}| \simeq 40.5$ vs $\Delta F_y = |F_y^{\text{in}} - F_y^{\text{out}}| \simeq 27.7 k_B T / \sigma$ for $\phi = 0.1$, and $\Delta F_x \simeq 21.95$ vs $\Delta F_y \simeq 17.87 k_B T / \sigma$ for $\phi = 0.3$. Other parameters: $D/\sigma = 3$, $\theta = 30^\circ$, and $F_{\text{sp}} = 20 k_B T / \sigma$. In these examples, the horizontal forces are repulsive, and the perpendicular force acting on the right (left) intruder is upward (downward).

pendicular direction on the inner and outer halves of each intruder ($\Delta F_y = |F_y^{\text{in}} - F_y^{\text{out}}| > 0$). The resulting torques due to ΔF_x and ΔF_y have opposite directions but cannot cancel each other since $\Delta F_x > \Delta F_y$. Therefore, the intruders rotate opposite to the direction of the active bath particles; see examples in Fig. 5.

In summary, we have elucidated how the interplay between stochastic forward propulsion and chirality results in long-range fluctuation-induced forces between objects immersed in chiral active fluids. Our findings demonstrate that the length scale and magnitude of the FI force can be enhanced significantly by optimizing the chirality. Such effective forces are capable of contributing to self-organization and assembly in active matter systems, particularly by affecting biological processes at microscales; for instance, stress fluctuations in actomyosin gels give rise to an effective attraction towards the boundaries of the confining domain [10], or dynamic active cytoskeletal forces may provide the driving force for nuclear fluctuations [11]. Our results open up avenues to explore structure formation in systems with active chiral constituents, such as biofilms and active chiral crystals, and may be exploited for design of micro-devices.

Simulation method. Each active composite is composed of 8 contacting spherical beads with diameter σ . The rodlike composites have a length of 8σ and the circular ones have a radius of $\sim 1.3\sigma$. The unequal covered area by the two types of composites requires that a different numbers of them be used to achieve a given occupied area fraction. The size of the simulation box is $L = 100\sigma$. The Lennard-Jones potential in Eq. (1) between interacting particles with center-to-center distance d is defined as

$$U_{\text{LJ}}(d) = 4\epsilon \left[\left(\frac{\sigma}{d} \right)^{12} - \left(\frac{\sigma}{d} \right)^6 \right], \quad (3)$$

where ϵ is the potential well depth. The mass of each bead M , its diameter σ , and the potential depth ϵ are chosen as the

units of mass, length, and energy, respectively. The solvent friction is $\eta = 10$ in all simulations. The Langevin dynamics simulations are carried using the LAMMPS code [55, 56]. The integration time step is taken to be $10^{-4} \tau$, with $\tau = \sqrt{M\sigma^2/\epsilon}$ being the simulation time unit. Before starting to measure the FI forces, we wait for 10^7 time steps to reach the steady state in the presence of active forces. Next, the mean FI force acting on each intruder during 10 time steps is measured. This quantity is averaged over 10^4 successive time intervals. The process of measuring the time-averaged forces are repeated over an ensemble of 10^2 uncorrelated trajectories for a further reduction of the fluctuations.

We thank Rudolf Podgornik for reading the manuscript. M.R.S. acknowledges support by the Deutsche Forschungsgemeinschaft (DFG) through Collaborative Research Center SFB 1027.

-
- [1] M. E. Cates and J. Tailleur, *Annu. Rev. Condens. Matter Phys.* **6**, 219 (2015).
- [2] T. Vicsek and A. Zafeiris, *Phys. Rep.* **517**, 71 (2012).
- [3] M. R. Shaebani, A. Wysocki, R. G. Winkler, G. Gompper, and H. Rieger, *Nat. Rev. Phys.* **2**, 181 (2020).
- [4] J. Elgeti, R. G. Winkler, and G. Gompper, *Rep. Prog. Phys.* **78**, 056601 (2015).
- [5] J. Stenhammar et al., *Phys. Rev. Lett.* **114**, 018301 (2015).
- [6] J. Schwarz-Linek, C. Valeriani, A. Cacciuto, M. E. Cates, D. Marenduzzo, A. N. Morozov, and W. C. K. Poon, *Proc. Natl. Acad. Sci. USA* **109**, 4052 (2012).
- [7] S. Gokhale, J. Li, A. Solon, J. Gore, and N. Fakhri, *Phys. Rev. E* **105**, 054605 (2022).
- [8] S. Paul, A. Jayaram, N. Narinder, T. Speck, and C. Bechinger, *Phys. Rev. Lett.* **129**, 058001 (2022).
- [9] Y. B. Dor, Y. Kafri, M. Kardar, and J. Tailleur, *Phys. Rev. E* **106**, 044604 (2022).
- [10] J.-F. Rupprecht, A. Singh Vishen, G. V. Shivashankar, M. Rao, and J. Prost, *Phys. Rev. Lett.* **120**, 098001 (2018).
- [11] E. Makhija, D. S. Jikhun, and G. V. Shivashankar, *Proc. Natl. Acad. Sci. USA* **113**, E32 (2016).
- [12] W. R. DiLuzio, L. Turner, M. Mayer, P. Garstecki, D. B. Weibel, H. C. Berg, and G. M. Whitesides, *Nature* **435**, 1271 (2005).
- [13] E. Lauga, W. R. DiLuzio, G. M. Whitesides, and H. A. Stone, *Biophys. J.* **90**, 400 (2006).
- [14] G. Li, L.-K. Tam, and J. X. Tang, *Proc. Natl. Acad. Sci. USA* **105**, 18355 (2008).
- [15] E. Perez Ipina, S. Otte, R. Pontier-Bres, D. Czerucka, and F. Peruani, *Nat. Phys.* **15**, 610 (2019).
- [16] R. Di Leonardo, D. Dell'Arciprete, L. Angelani, and V. Iebba, *Phys. Rev. Lett.* **106**, 038101 (2011).
- [17] G. Jékely, J. Colombelli, H. Hausen, K. Guy, E. Stelzer, F. Nédélec, and D. Arendt, *Nature* **456**, 395 (2008).
- [18] T.-W. Su, L. Xue, and A. Ozcan, *Proc. Natl. Acad. Sci. USA* **109**, 16018 (2012).
- [19] B. M. Friedrich and F. JÁzlicher, *Proc. Natl. Acad. Sci. USA* **104**, 13256 (2007).
- [20] F. Kümmel, B. ten Hagen, R. Wittkowski, I. Buttinoni, R. Eichhorn, G. Volpe, H. Löwen, and C. Bechinger, *Phys. Rev. Lett.* **110**, 198302 (2013).
- [21] B. ten Hagen, F. Kümmel, R. Wittkowski, D. Takagi, H. Löwen, and C. Bechinger, *Nat. Commun.* **5**, 4829 (2014).
- [22] P. Arora, A. K. Sood, and R. Ganapathy, *Sci. Adv.* **7**, eabd0331 (2021).
- [23] M. R. Shaebani, R. Jose, L. Santen, L. Stankevics, and F. Lautenschläger, *Phys. Rev. Lett.* **125**, 268102 (2020).
- [24] M. R. Shaebani, M. Piel, and F. Lautenschläger, *Biophys. J.* **121**, 4099 (2022).
- [25] J. Najafi et al., *Sci. Adv.* **4**, eaar6425 (2018).
- [26] Q. Yang, H. Zhu, P. Liu, R. Liu, Q. Shi, K. Chen, N. Zheng, F. Ye, and M. Yang, *Phys. Rev. Lett.* **126**, 198001 (2021).
- [27] J. L. Aragonés, J. P. Steimel, and A. Alexander-Katz, *Nat. Commun.* **7**, 11325 (2016).
- [28] A. Aminov, Y. Kafri, and M. Kardar, *Phys. Rev. Lett.* **114**, 230602 (2015).
- [29] A. A. Lee, D. Vella, and J. S. Wettlaufer, *Proc. Natl. Acad. Sci. USA* **114**, 9255 (2017).
- [30] B. Liebchen and D. Levis, *Phys. Rev. Lett.* **119**, 058002 (2017).
- [31] B. Liebchen and D. Levis, *Europhys. Lett.* **139**, 67001 (2022).
- [32] M. R. Shaebani, J. Sarabadani, and D. E. Wolf, *Phys. Rev. Lett.* **108**, 198001 (2012).
- [33] C. Cattuto, R. Brito, U. M. B. Marconi, F. Nori, and R. Soto, *Phys. Rev. Lett.* **96**, 178001 (2006).
- [34] M. R. Shaebani, J. Sarabadani, and D. E. Wolf, *Phys. Rev. E* **88**, 022202 (2013).
- [35] R. Ni, M. A. Cohen Stuart, and P. G. Bolhuis, *Phys. Rev. Lett.* **114**, 018302 (2015).
- [36] L. R. Leite, D. Lucena, F. Q. Potiguar, and W. P. Ferreira, *Phys. Rev. E* **94**, 062602 (2016).
- [37] D. Ray, C. Reichhardt, and C. J. O. Reichhardt, *Phys. Rev. E* **90**, 013019 (2014).
- [38] F. Feng, T. Lei, and N. Zhao, *Phys. Rev. E* **103**, 022604 (2021).
- [39] L. Angelani et al., *Phys. Rev. Lett.* **107**, 138302 (2011).
- [40] P. Liu, S. Ye, F. Ye, K. Chen, and M. Yang, *Phys. Rev. Lett.* **124**, 158001 (2020).
- [41] J. Harder, S. A. Mallory, C. Tung, C. Valeriani, and A. Cacciuto, *J. Chem. Phys.* **141**, 194901 (2014).
- [42] Y. Baek, A. P. Solon, X. Xu, N. Nikola, and Y. Kafri, *Phys. Rev. Lett.* **120**, 058002 (2018).
- [43] C. Parra-Rojas and R. Soto, *Phys. Rev. E* **90**, 013024 (2014).
- [44] R. D. Leonardo, L. Angelani, D. Dell'Arciprete, G. Ruocco, V. Iebba, S. Schippa, M. P. Conte, F. Mecarini, F. D. Angelis, and E. D. Fabrizio, *Proc. Natl. Acad. Sci. USA* **107**, 9541 (2010).
- [45] BC van Zuiden et al., *Proc. Natl. Acad. Sci. USA* **113**, 12919 (2016).
- [46] T. H. Tan, A. Mietke, J. Li, Y. Chen, H. Higinbotham, P. J. Foster, S. Gokhale, J. Dunkel, and N. Fakhri, *Nature* **607**, 287 (2022).
- [47] A. P. Petroff, X.-L. Wu, and A. Libchaber, *Phys. Rev. Lett.* **114**, 158102 (2015).
- [48] D. Chandler, J. D. Weeks, and H. C. Andersen, *Science* **220**, 787 (1983).
- [49] R. Nossal and G. H. Weiss, *J. Theor. Biol.* **47**, 103 (1974).
- [50] M. R. Shaebani and H. Rieger, *Front. Phys.* **7**, 120 (2019).

- [51] M. R. Shaebani, H. Rieger, and Z. Sadjadi, Phys. Rev. E **106**, 034105 (2022).
- [52] Z. Sadjadi and M. R. Shaebani, Phys. Rev. E **104**, 054613 (2021).
- [53] B. Zhang and A. Snezhko, Phys. Rev. Lett. **128**, 218002 (2022).
- [54] A. Torrik, A. Naji, and M. Zarif, Phys. Rev. E **104**, 064610 (2021).
- [55] <http://lammmps.sandia.gov/> (LAMMPS molecular dynamics simulator).
- [56] S. Plimpton, J. Comput. Phys. **117**, 1 (1995).